

# Search for anomalous weak dipole moments of the $\tau$ lepton

The ALEPH Collaboration

A. Heister, S. Schael

Physikalisches Institut des RWTH-Aachen, 52056 Aachen, Germany

R. Barate, I. De Bonis, D. Decamp, C. Goy, J.-P. Lees, E. Merle, M.-N. Minard, B. Pietrzyk  
Laboratoire de Physique des Particules (LAPP), IN<sup>2</sup>P<sup>3</sup>-CNRS, 74019 Annecy-le-Vieux Cedex, France

S. Bravo, M.P. Casado, M. Chmeissani, J.M. Crespo, E. Fernandez, M. Fernandez-Bosman, Ll. Garrido,<sup>15</sup>  
M. Martinez, A. Pacheco, H. Ruiz  
Institut de Física d'Altes Energies, Universitat Autònoma de Barcelona, 08193 Bellaterra (Barcelona), Spain<sup>7</sup>

A. Colaleo, D. Creanza, M. de Palma, G. Iaselli, G. Maggi, M. Maggi, S. Nuzzo, A. Ranieri, G. Raso,<sup>23</sup> F. Ruggieri,  
G. Selvaggi, L. Silvestris, P. Tempesta, A. Tricomi,<sup>3</sup> G. Zito  
Dipartimento di Fisica, INFN Sezione di Bari, 70126 Bari, Italy

X. Huang, J. Lin, Q. Ouyang, T. Wang, Y. Xie, R. Xu, S. Xue, J. Zhang, L. Zhang, W. Zhao  
Institute of High Energy Physics, Academia Sinica, Beijing, P.R. China<sup>8</sup>

D. Abbaneo, P. Azzurri, O. Buchmüller,<sup>25</sup> M. Cattaneo, F. Cerutti, B. Clerbaux,<sup>28</sup> H. Drevermann, R.W. Forty,  
M. Frank, F. Gianotti, J.B. Hansen, J. Harvey, D.E. Hutchcroft, P. Janot, B. Jost, M. Kado,<sup>27</sup> P. Mato, A. Moutoussi,  
F. Ranjard, L. Rolandi, D. Schlatter, O. Schneider,<sup>2</sup> G. Sguazzoni, W. Tejessy, F. Teubert, A. Valassi, I. Videau,  
J. Ward  
European Laboratory for Particle Physics (CERN), 1211 Geneva 23, Switzerland

F. Badaud, A. Falvard,<sup>22</sup> P. Gay, P. Henrard, J. Jousset, B. Michel, S. Monteil, J.-C. Montret, D. Pallin, P. Perret  
Laboratoire de Physique Corpusculaire, Université Blaise Pascal, IN<sup>2</sup>P<sup>3</sup>-CNRS, Clermont-Ferrand, 63177 Aubière, France

J.D. Hansen, J.R. Hansen, P.H. Hansen, B.S. Nilsson  
Niels Bohr Institute, 2100 Copenhagen, Denmark<sup>9</sup>

A. Kyriakis, C. Markou, E. Simopoulou, A. Vayaki, K. Zachariadou  
Nuclear Research Center Demokritos (NRCD), 15310 Attiki, Greece

A. Blondel,<sup>12</sup> G. Bonneaud, J.-C. Brient, A. Rougé, M. Rumpf, M. Swynghedauw, M. Verderi,  
H. Videau  
Laboratoire Leprince-Ringuet, Ecole Polytechnique, IN<sup>2</sup>P<sup>3</sup>-CNRS, 91128 Palaiseau Cedex, France

V. Ciulli, E. Focardi, G. Parrini  
Dipartimento di Fisica, Università di Firenze, INFN Sezione di Firenze, 50125 Firenze, Italy

A. Antonelli, M. Antonelli, G. Bencivenni, F. Bossi, G. Capon, V. Chiarella, P. Laurelli, G. Mannocchi,<sup>5</sup> G.P. Murtas,  
L. Passalacqua, M. Pepe-Altarelli<sup>4</sup>  
Laboratori Nazionali dell'INFN (LNF-INFN), 00044 Frascati, Italy

J.G. Lynch, P. Negus, V. O'Shea, C. Raine,<sup>6</sup> A.S. Thompson  
Department of Physics and Astronomy, University of Glasgow, Glasgow G12 8QQ, UK<sup>10</sup>

S. Wasserbaech  
Department of Physics, Haverford College, Haverford, PA 19041-1392, USA

R. Cavanaugh,<sup>21</sup> C. Geweniger, P. Hanke, V. Hepp, E.E. Kluge, A. Putzer, H. Stenzel, K. Tittel, M. Wunsch<sup>19</sup>  
Kirchhoff-Institut für Physik, Universität Heidelberg, 69120 Heidelberg, Germany<sup>16</sup>

R. Beuselinck, D.M. Binnie, W. Cameron, P.J. Dornan, M. Girone,<sup>1</sup> N. Marinelli, J.K. Sedgbeer, J.C. Thompson<sup>14</sup>  
Department of Physics, Imperial College, London SW7 2BZ, UK<sup>10</sup>

V.M. Ghete, P. Girtler, E. Kneringer, D. Kuhn, G. Rudolph

Institut für Experimentalphysik, Universität Innsbruck, 6020 Innsbruck, Austria<sup>18</sup>

E. Bouhova-Thacker, C.K. Bowdery, A.J. Finch, F. Foster, G. Hughes, R.W.L. Jones, M.R. Pearson, N.A. Robertson  
Department of Physics, University of Lancaster, Lancaster LA1 4YB, UK<sup>10</sup>

K. Jakobs, K. Kleinknecht, B. Renk, H.-G. Sander, H. Wachsmuth, C. Zeitnitz

Institut für Physik, Universität Mainz, 55099 Mainz, Germany<sup>16</sup>

A. Bonissent, P. Coyle, O. Leroy, P. Payre, D. Rousseau, M. Talby

Centre de Physique des Particules, Université de la Méditerranée, IN<sup>2</sup>P<sup>3</sup>-CNRS, 13288 Marseille, France

F. Ragusa

Dipartimento di Fisica, Università di Milano e INFN Sezione di Milano, 20133 Milano, Italy

A. David, H. Dietl, G. Ganis,<sup>26</sup> K. Hüttmann, G. Lütjens, W. Männer, H.-G. Moser, R. Settles, W. Wiedenmann, G. Wolf

Max-Planck-Institut für Physik, Werner-Heisenberg-Institut, 80805 München, Germany<sup>16</sup>

J. Boucrot, O. Callot, M. Davier, L. Duflot, J.-F. Grivaz, Ph. Heusse, A. Jacholkowska,<sup>24</sup> J. Lefrançois, J.-J. Veillet, C. Yuan

Laboratoire de l'Accélérateur Linéaire, Université de Paris-Sud, IN<sup>2</sup>P<sup>3</sup>-CNRS, 91898 Orsay Cedex, France

G. Bagliesi, T. Boccali, L. Foà, A. Giammanco, A. Giassi, F. Ligabue, A. Messineo, F. Palla, G. Sanguinetti, A. Sciabà, R. Tenchini,<sup>1</sup> A. Venturi,<sup>1</sup> P.G. Verdini

Dipartimento di Fisica dell'Università, INFN Sezione di Pisa, e Scuola Normale Superiore, 56010 Pisa, Italy

G.A. Blair, G. Cowan, M.G. Green, T. Medcalf, A. Misiejuk, J.A. Strong, P. Teixeira-Dias,

Department of Physics, Royal Holloway & Bedford New College, University of London, Egham, Surrey TW20 OEX, UK<sup>10</sup>

R.W. Clift, T.R. Edgecock, P.R. Norton, I.R. Tomalin

Particle Physics Dept., Rutherford Appleton Laboratory, Chilton, Didcot, Oxon OX11 0QX, UK<sup>10</sup>

B. Bloch-Devaux, P. Colas, E. Lançon, M.-C. Lemaire, E. Locci, P. Perez, J. Rander, J.-P. Schuller, B. Vallage  
CEA, DAPNIA/Service de Physique des Particules, CE-Saclay, 91191 Gif-sur-Yvette Cedex, France<sup>17</sup>

N. Konstantinidis, A.M. Litke, G. Taylor

Institute for Particle Physics, University of California at Santa Cruz, Santa Cruz, CA 95064, USA<sup>13</sup>

C.N. Booth, S. Cartwright, F. Combley,<sup>6</sup> M. Lehto, L.F. Thompson

Department of Physics, University of Sheffield, Sheffield S3 7RH, UK<sup>10</sup>

A. Böhrer, S. Brandt, C. Grupen, A. Ngac, G. Prange,

Fachbereich Physik, Universität Siegen, 57068 Siegen, Germany<sup>16</sup>

G. Giannini

Dipartimento di Fisica, Università di Trieste e INFN Sezione di Trieste, 34127 Trieste, Italy

J. Rothberg

Experimental Elementary Particle Physics, University of Washington, Seattle, WA 98195 USA

S.R. Armstrong, K. Berkelman, K. Cranmer, D.P.S. Ferguson, Y. Gao,<sup>20</sup> S. González, O.J. Hayes, H. Hu, S. Jin, J. Kile, P.A. McNamara III, J. Nielsen, Y.B. Pan, J.H. von Wimmersperg-Toeller, W. Wiedenmann, J. Wu, Sau Lan Wu, X. Wu, G. Zobernig

Department of Physics, University of Wisconsin, Madison, WI 53706, USA<sup>11</sup>

G. Dissertori

Institute for Particle Physics, ETH Hönggerberg, 8093 Zürich, Switzerland

Received: 25 September 2002 /

Published online: 29 August 2003 – © Springer-Verlag / Società Italiana di Fisica 2003

**Abstract.** The anomalous weak dipole moments of the  $\tau$  lepton are measured in a data sample collected by ALEPH from 1990 to 1995 corresponding to an integrated luminosity of  $155 \text{ pb}^{-1}$ . Tau leptons produced in the reaction  $e^+e^- \rightarrow \tau^+\tau^-$  at energies close to the Z mass are studied using their semileptonic decays to  $\pi$ ,  $\rho$ ,  $a_1 \rightarrow \pi 2\pi^0$  or  $a_1 \rightarrow 3\pi$ . The real and imaginary components of both the anomalous weak magnetic dipole

moment and the CP-violating anomalous weak electric dipole moment,  $\text{Re } \mu_\tau$ ,  $\text{Im } \mu_\tau$ ,  $\text{Re } d_\tau$  and  $\text{Im } d_\tau$ , are measured simultaneously by means of a likelihood fit built from the full differential cross section. No evidence of new physics is found. The following bounds are obtained (95% CL):  $|\text{Re } \mu_\tau| < 1.14 \times 10^{-3}$ ,  $|\text{Im } \mu_\tau| < 2.65 \times 10^{-3}$ ,  $|\text{Re } d_\tau| < 0.91 \times 10^{-3}$ , and  $|\text{Im } d_\tau| < 2.01 \times 10^{-3}$ .

## 1 Introduction

The anomalous weak dipole moments of the  $\tau$  lepton are the tensorial couplings of the  $Z\tau^+\tau^-$  vertex. They are zero to first order in the Standard Model (SM). Two types of anomalous weak dipole moments can be distinguished: the magnetic term  $\mu_\tau$  and the CP-violating electric term  $d_\tau$ . Here, both the real and the imaginary components of each anomalous weak dipole moment are explored, i.e.  $\text{Re } \mu_\tau$ ,

$\text{Im } \mu_\tau$ ,  $\text{Re } d_\tau$  and  $\text{Im } d_\tau$ . Radiative corrections in the SM provide nonzero predictions for  $\mu_\tau$  and  $d_\tau$  [1,2] which are below the present experimental sensitivity. This opens the possibility to look for deviations from the SM.

There have been many searches for the CP-violating anomalous weak electric dipole moment of the  $\tau$  since the beginning of LEP [3-5]. In addition, limits on the anomalous weak magnetic dipole moment were obtained more recently [5].

In this analysis, the previous ALEPH result on  $\text{Re } d_\tau$  [3] is updated, and  $\text{Re } \mu_\tau$ ,  $\text{Im } \mu_\tau$  and  $\text{Im } d_\tau$  are determined for the first time in ALEPH. The data sample was collected with the ALEPH detector from 1990 to 1995 at energies around the Z resonance and corresponds to an integrated luminosity of  $155 \text{ pb}^{-1}$ . Tau leptons are generated in the reaction  $e^+e^- \rightarrow \tau^+\tau^-$  at LEP. The method to extract the anomalous weak dipole moments is based on a maximum likelihood fit to the data taking into account all  $\tau$  spin terms explicitly, including correlations. This is the first time that the complete differential cross section for the production and decay of the  $\tau$  leptons is considered to estimate the  $\tau$  anomalous weak dipole moments. The most important semileptonic decays are used:  $\pi$ ,  $\rho$ ,  $a_1 \rightarrow \pi 2\pi^0$  and  $a_1 \rightarrow 3\pi$ . The  $\tau$  spin information is recovered using optimal polarimeters which are different for each decay. The selection and particle identification make use of tools already developed in previous analyses [6-9].

The text is organized as follows. The theoretical framework is introduced in Sect. 2. The most important ALEPH subdetectors for this analysis are covered in Sect. 3. The data analysis procedure is explained in Sect. 4, emphasizing the new features of the analysis. The more relevant systematic uncertainties are then discussed in Sect. 5. The results and conclusions are presented in Sect. 6.

## 2 Theoretical framework

### 2.1 Production cross section

The currents assumed for photon and Z exchange in  $e^+e^- \rightarrow \tau^+\tau^-$  production are

$$\begin{aligned} \Gamma_f^{\mu(\gamma)} &= iQ_f e \gamma^\mu, \quad \text{with } f = e, \tau, \\ \Gamma_e^{\mu(Z)} &= ie [v_e \gamma^\mu - a_e \gamma^\mu \gamma_5], \\ \Gamma_\tau^{\mu(Z)} &= ie \left[ v_\tau \gamma^\mu - a_\tau \gamma^\mu \gamma_5 + i \frac{\mu_\tau}{2m_\tau} \sigma^{\mu\nu} q_\nu \right. \\ &\quad \left. + \frac{d_\tau}{2m_\tau} \gamma_5 \sigma^{\mu\nu} q_\nu \right], \end{aligned} \quad (1)$$

where  $Q_f e$  is the fermion charge;  $a_e$ ,  $a_\tau$ ,  $v_e$  and  $v_\tau$  are the axial vector and vector couplings of the SM;  $\mu_\tau$  and  $d_\tau$  are

<sup>1</sup> Also at CERN, 1211 Geneva 23, Switzerland

<sup>2</sup> Now at Université de Lausanne, 1015 Lausanne, Switzerland

<sup>3</sup> Also at Dipartimento di Fisica di Catania and INFN Sezione di Catania, 95129 Catania, Italy

<sup>4</sup> Now at CERN, 1211 Geneva 23, Switzerland

<sup>5</sup> Also Istituto di Cosmo-Geofisica del C.N.R., Torino, Italy

<sup>6</sup> Deceased

<sup>7</sup> Supported by CICYT, Spain

<sup>8</sup> Supported by the National Science Foundation of China

<sup>9</sup> Supported by the Danish Natural Science Research Council

<sup>10</sup> Supported by the UK Particle Physics and Astronomy Research Council

<sup>11</sup> Supported by the US Department of Energy, grant DE-FG0295-ER40896

<sup>12</sup> Now at Departement de Physique Corpusculaire, Université de Genève, 1211 Genève 4, Switzerland

<sup>13</sup> Supported by the US Department of Energy, grant DE-FG03-92ER40689

<sup>14</sup> Supported by the Leverhulme Trust

<sup>15</sup> Permanent address: Universitat de Barcelona, 08208 Barcelona, Spain

<sup>16</sup> Supported by Bundesministerium für Bildung und Forschung, Germany

<sup>17</sup> Supported by the Direction des Sciences de la Matière, C.E.A.

<sup>18</sup> Supported by the Austrian Ministry for Science and Transport

<sup>19</sup> Now at SAP AG, 69185 Walldorf, Germany

<sup>20</sup> Also at Department of Physics, Tsinghua University, Beijing, The People's Republic of China

<sup>21</sup> Now at University of Florida, Department of Physics, Gainesville, Florida 32611-8440, USA

<sup>22</sup> Now at Groupe d'Astroparticules de Montpellier, Université de Montpellier II, 34095, Montpellier, France

<sup>23</sup> Also at Dipartimento di Fisica e Tecnologia Relative, Università di Palermo, Palermo, Italy

<sup>24</sup> Also at Groupe d'Astroparticules de Montpellier, Université de Montpellier II, 34095, Montpellier, France

<sup>25</sup> Now at SLAC, Stanford, CA 94309, USA

<sup>26</sup> Now at INFN Sezione di Roma II, Dipartimento di Fisica, Università di Roma Tor Vergata, 00133 Roma, Italy

<sup>27</sup> Now at Fermilab, PO Box 500, MS 352, Batavia, IL 60510, USA

<sup>28</sup> Now at Institut Inter-universitaire des Hautes Energies (IHE), CP 230, Université Libre de Bruxelles, 1050 Bruxelles, Belgique

the anomalous weak magnetic and anomalous weak electric dipole moments of the  $\tau$ . In the previous expression both anomalous weak dipole moments are dimensionless quantities. However, the anomalous weak electric dipole moment is often quoted in the literature in units of e cm, by defining the contribution of this dipole moment to the current as  $id_\tau\gamma_5\sigma^{\mu\nu}q_\nu$ . These different notations are related by the conversion factor  $e/2m_\tau = 5.552 \times 10^{-15}$  e cm.

Using the currents in (1), the differential cross section can be expressed as [10]

$$\frac{d\sigma}{d\cos\theta_\tau}(\vec{s}_1, \vec{s}_2) = R_{00} + \sum_{\mu=1,3} R_{\mu 0} s_1^\mu + \sum_{\nu=1,3} R_{0\nu} s_2^\nu + \sum_{\mu,\nu=1,3} R_{\mu\nu} s_1^\mu s_2^\nu. \quad (2)$$

The  $R_{\mu\nu}$  terms are functions of the fermion couplings and of the  $\tau$  production angle  $\theta_\tau$ ;  $\vec{s}_1$  and  $\vec{s}_2$  are unit vectors chosen as the quantisation axes for the spin measurement of the  $\tau^+$  and the  $\tau^-$ , respectively, in their corresponding rest frames.

The following reference frame has been chosen: the  $z$  axis is in the outgoing  $\tau^+$  direction and the incoming  $e^+$  is in the  $yz$  plane. The  $x$  component is therefore normal to the production plane. The  $y$  component is called transverse.

Several  $R_{\mu\nu}$  terms have been already measured by ALEPH. Defining  $(R_{\mu\nu})_\pm \equiv (R_{\mu\nu} \pm R_{\nu\mu})$ , these terms are the following:

- $R_{00} = d\sigma/d\cos\theta_\tau$  [11],
- $(R_{03})_+/R_{00} = P_\tau(\cos\theta_\tau)$  is the longitudinal polarisation of the  $\tau$  [9],
- $R_{22}/R_{00} = -R_{11}/R_{00}$  are the transverse-transverse and normal-normal spin correlations [12],
- $(R_{21})_+/R_{00}$  are the transverse-normal spin correlations [12].

The  $R_{\mu\nu}$  terms most sensitive to  $\text{Re}\mu_\tau$ ,  $\text{Im}\mu_\tau$ ,  $\text{Re}d_\tau$  and  $\text{Im}d_\tau$  are presented below. These terms are obtained from [10] after some algebra. The SM contributions are separated from the anomalous (anm) contributions.

$\text{Re}\mu_\tau$ :

$$\begin{aligned} (R_{02})_+|_{\text{SM}} &\propto \frac{2}{\gamma_\tau} \sin\theta_\tau |v_\tau|^2 \text{Re}(v_e a_e^*) \\ &\quad + \frac{1}{\gamma_\tau} \sin\theta_\tau \cos\theta_\tau (|a_e|^2 + |v_e|^2) \text{Re}(v_\tau a_\tau^*) \\ (R_{02})_+|_{\text{anm}} &\propto \gamma_\tau \sin\theta_\tau \cos\theta_\tau (|a_e|^2 + |v_e|^2) \text{Re}(a_\tau \mu_\tau^*) \\ &\quad + \frac{2(\gamma_\tau^2 + 1)}{\gamma_\tau} \sin\theta_\tau \text{Re}(v_e a_e^*) \text{Re}(v_\tau \mu_\tau^*) \\ &\quad + 2\gamma_\tau \sin\theta_\tau \text{Re}(v_e a_e^*) |\mu_\tau|^2 \\ (R_{32})_+|_{\text{SM}} &\propto \frac{2}{\gamma_\tau} \sin\theta_\tau \text{Re}(v_e a_e^*) \text{Re}(v_\tau a_\tau^*) \\ &\quad + \frac{1}{\gamma_\tau} \sin\theta_\tau \cos\theta_\tau (|a_e|^2 + |v_e|^2) |v_\tau|^2 \\ (R_{32})_+|_{\text{anm}} &\propto \frac{\gamma_\tau^2 + 1}{\gamma_\tau} \sin\theta_\tau \cos\theta_\tau (|a_e|^2 + |v_e|^2) \text{Re}(v_\tau \mu_\tau^*) \end{aligned} \quad (3)$$

$$\begin{aligned} &+ 2\gamma_\tau \sin\theta_\tau \text{Re}(v_e a_e^*) \text{Re}(a_\tau \mu_\tau^*) \\ &+ \gamma_\tau \sin\theta_\tau \cos\theta_\tau (|a_e|^2 + |v_e|^2) |\mu_\tau|^2 \end{aligned} \quad (4)$$

$\text{Im}\mu_\tau$ :

$$\begin{aligned} (R_{31})_+|_{\text{SM}} &\propto \frac{1}{\gamma_\tau} \sin\theta_\tau \cos\theta_\tau (|a_e|^2 + |v_e|^2) \text{Im}(v_\tau a_\tau^*) \\ (R_{31})_+|_{\text{anm}} &\propto \gamma_\tau \sin\theta_\tau \cos\theta_\tau (|a_e|^2 + |v_e|^2) \text{Im}(a_\tau \mu_\tau^*) \\ &\quad + \frac{2(\gamma_\tau^2 - 1)}{\gamma_\tau} \sin\theta_\tau \text{Re}(v_e a_e^*) \text{Im}(v_\tau \mu_\tau^*) \\ (R_{01})_+|_{\text{SM}} &\propto \frac{2}{\gamma_\tau} \sin\theta_\tau \text{Re}(v_e a_e^*) \text{Im}(v_\tau a_\tau^*) \\ (R_{01})_+|_{\text{anm}} &\propto \frac{\gamma_\tau^2 - 1}{\gamma_\tau} \sin\theta_\tau \cos\theta_\tau (|a_e|^2 + |v_e|^2) \text{Im}(v_\tau \mu_\tau^*) \\ &\quad + 2\gamma_\tau \sin\theta_\tau \text{Re}(v_e a_e^*) \text{Im}(a_\tau \mu_\tau^*) \end{aligned} \quad (5)$$

$\text{Re}d_\tau$ :

$$\begin{aligned} (R_{01})_-|_{\text{SM}} &= 0 \\ (R_{01})_-|_{\text{anm}} &\propto -\gamma_\tau \sin\theta_\tau \cos\theta_\tau (|a_e|^2 + |v_e|^2) \text{Re}(a_\tau d_\tau^*) \\ &\quad - 2\gamma_\tau \sin\theta_\tau \text{Re}(v_e a_e^*) \\ &\quad \times [\text{Re}(v_\tau d_\tau^*) + \text{Re}(\mu_\tau d_\tau^*)] \\ (R_{31})_-|_{\text{SM}} &= 0 \\ (R_{31})_-|_{\text{anm}} &\propto -\gamma_\tau \sin\theta_\tau \cos\theta_\tau (|a_e|^2 + |v_e|^2) \\ &\quad \times [\text{Re}(v_\tau d_\tau^*) + \text{Re}(\mu_\tau d_\tau^*)] \\ &\quad - 2\gamma_\tau \sin\theta_\tau \text{Re}(v_e a_e^*) \text{Re}(a_\tau d_\tau^*) \end{aligned} \quad (7)$$

$\text{Im}d_\tau$ :

$$\begin{aligned} (R_{32})_-|_{\text{SM}} &= 0 \\ (R_{32})_-|_{\text{anm}} &\propto \gamma_\tau \sin\theta_\tau \cos\theta_\tau (|a_e|^2 + |v_e|^2) \text{Im}(a_\tau d_\tau^*) \\ &\quad + 2\gamma_\tau \sin\theta_\tau \text{Re}(v_e a_e^*) \\ &\quad \times [\text{Im}(v_\tau d_\tau^*) + \text{Im}(\mu_\tau d_\tau^*)] \\ (R_{02})_-|_{\text{SM}} &= 0 \\ (R_{02})_-|_{\text{anm}} &\propto \gamma_\tau \sin\theta_\tau \cos\theta_\tau (|a_e|^2 + |v_e|^2) \\ &\quad \times [\text{Im}(v_\tau d_\tau^*) + \text{Im}(\mu_\tau d_\tau^*)] \\ &\quad + 2\gamma_\tau \sin\theta_\tau \text{Re}(v_e a_e^*) \text{Im}(a_\tau d_\tau^*) \end{aligned} \quad (9)$$

Taking into account that  $a_l \gg v_l$ , the terms can be ordered in sensitivity, and the most sensitive term for each anomalous weak dipole moment is presented first. The quantity  $\gamma_\tau$  is computed as  $\sqrt{s}/2m_\tau$ . The photon exchange terms are omitted from these expressions for simplicity, although they are taken into account in the final results.

The anomalous weak dipole moments are extracted including all  $R_{\mu\nu}$  terms in a maximum likelihood fit. In this analysis  $(R_{31})_+$ , the most sensitive term to  $\text{Im}\mu_\tau$ , is used for the first time as proposed in [13]. The terms  $(R_{02})_+$ ,  $(R_{01})_-$  and  $(R_{32})_-$  were previously used in other measurements of the anomalous weak dipole moments.

## 2.2 Tau decay

For each  $\tau$  decay mode, the differential partial width of a polarised  $\tau$  is written as

$$d\Gamma(\vec{s}) = W(1 + \vec{h} \cdot \vec{s}) dX, \quad (11)$$

using the expressions for  $W$  and  $\vec{h}$  from the TAUOLA Monte Carlo program [14];  $W$  is the differential partial width of an unpolarised  $\tau$ , and the  $\vec{h}$  vector is the polarimeter of the particular decay mode considered. Both  $W$  and  $\vec{h}$  depend on the four-momenta of the final state particles in the  $\tau$  rest frame, and they are different for each decay topology. The simplest expressions are those of the  $\tau$  decay into  $\pi$ . In this case,  $\vec{h}_\pi$  is proportional to the  $\pi$  momentum in the  $\tau$  rest frame and  $W_\pi$  is a constant. In the above equation,  $X$  is a set of independent variables describing the full decay configuration. The number of elements of the set depends on the number of particles in the final state. The set  $X_\pi$  denotes the set of variables expressing the  $\pi$  direction in the  $\tau$  rest frame.

In this analysis, the expressions for  $W$  and  $\vec{h}$  allow the spin information for all the  $\tau$  decays to be recovered optimally.

## 2.3 The full differential cross section

Once the production cross section and the partial decays are introduced, the full differential cross section of  $e^+e^- \rightarrow \tau^+\tau^- \rightarrow x_1^+x_2^-\bar{\nu}_\tau\nu_\tau$  is built following [15,16], namely

$$\frac{d\sigma}{d\cos\theta_\tau dX_1 dX_2} = 4 \frac{W_1}{\Gamma_\tau} \frac{W_2}{\Gamma_\tau} \times \left[ R_{00} + \sum_{\mu=1,3} R_{\mu 0} h_1^\mu + \sum_{\nu=1,3} R_{0\nu} h_2^\nu + \sum_{\mu,\nu=1,3} R_{\mu\nu} h_1^\mu h_2^\nu \right]. \quad (12)$$

In this equation  $\Gamma_\tau$  is the total  $\tau$  width,  $X_1$  and  $X_2$  are the sets of independent variables, and  $\vec{h}_1$  and  $\vec{h}_2$  are the polarimeters for the decay of the  $\tau^+$  and the  $\tau^-$ , respectively.

With the definitions  $\bar{R}_{\mu\nu} = R_{\mu\nu}/R_{00}$ ,  $H^\mu = W h^\mu / \Gamma_\tau$  ( $\mu, \nu = 0, \dots, 3$ ), and  $h^0 = 1$ , the likelihood of an event with the final state topology  $ij$  is written as

$$\begin{aligned} L_{ij}(\mu_\tau, d_\tau | \theta_\tau, W_1, \cos\theta_{h_1}, \phi_{h_1}, W_2, \cos\theta_{h_2}, \phi_{h_2}) \\ = \sum_{\mu,\nu=0,\dots,3} \bar{R}_{\mu\nu}(\mu_\tau, d_\tau, \theta_\tau) H_i^\mu(W_1, \cos\theta_{h_1}, \phi_{h_1}) \\ \times H_j^\nu(W_2, \cos\theta_{h_2}, \phi_{h_2}). \end{aligned} \quad (13)$$

The indices  $(i, j)$  refer to the decay mode of each  $\tau$ , with  $i, j = \pi, \rho, \pi 2\pi^0, 3\pi$ , and the quantities  $(W_1, \cos\theta_{h_1}, \phi_{h_1})$  and  $(W_2, \cos\theta_{h_2}, \phi_{h_2})$  are the observables related to the decay of the  $\tau^+$  and the  $\tau^-$ , respectively. The angles  $(\theta_{h_1}, \phi_{h_1}, \theta_{h_2}, \phi_{h_2})$  are the polar and azimuthal angles of the polarimeters of each  $\tau$ , in the reference frame introduced in Sect. 2.1. The above likelihood is also a function of the

centre-of-mass energy. The distributions of the hemisphere observables  $W$  and  $\cos\theta_h$  are presented in Figs. 1 and 2.

This likelihood fulfills the normalisation condition

$$\sum_{ij} \int L_{ij}(\mu_\tau, d_\tau | \theta_\tau, W_1, \cos\theta_{h_1}, \phi_{h_1}, W_2, \cos\theta_{h_2}, \phi_{h_2}) \times dX_1 dX_2 = 1. \quad (14)$$

This is the integral over all possible decay parameters and all possible decay topologies  $ij$  for a given  $e^+e^- \rightarrow \tau^+\tau^-$  event. The normalisation is such that the likelihood depends only upon the net spin polarisation of the produced  $\tau$  pairs, and not upon  $R_{00} = d\sigma/d\cos\theta_\tau$ .

## 3 Apparatus

The ALEPH detector is described in detail in [17] and its performance in [18].

Charged particles are measured with a high resolution silicon vertex detector (VDET), a cylindrical drift chamber (ITC), and a large time projection chamber (TPC). The momentum resolution in the axial magnetic field of 1.5 T provided by a superconducting solenoid is  $\Delta p/p^2 = 0.6 \times 10^{-3} (\text{GeV}/c)^{-1}$  for high momentum tracks. The impact parameter resolutions for high momentum tracks with hits in all three subdetectors are  $\sigma_{r\phi} = 23 \mu\text{m}$  and  $\sigma_z = 28 \mu\text{m}$ .

The tracking devices are surrounded by the electromagnetic calorimeter (ECAL), which is a highly segmented lead/proportional-wire-chamber calorimeter. The calorimeter is read out via cathode pads arranged in projective towers covering  $0.9^\circ \times 0.9^\circ$  in solid angle and summing the deposited energy in three sections of depth. A second readout is provided by the signals from the anode wires. The energy resolution dependence with energy can be represented as is  $\sigma/E = 0.009 + 0.18/\sqrt{E(\text{GeV})}$ .

The ECAL is inside the solenoid, which is followed by the hadron calorimeter (HCAL). Hadronic showers are sampled by 23 planes of streamer tubes giving a digital hit pattern and an analog signal on pads, which are also arranged in projective towers. This calorimeter is used in this analysis to discriminate between pions and muons. Outside the HCAL there are two layers of muon chambers providing additional information for  $\mu$  identification.

## 4 Data analysis

### 4.1 Selection and decay classification

Events from  $Z \rightarrow \tau^+\tau^-$  are retained using a global selection in which each event is divided into two hemispheres along the thrust axis. The selection is that used in the ALEPH measurement of  $P_\tau(\cos\theta_\tau)$  with the  $\tau$  direction method [9]. Additional information can be found in [8] and references therein.

The charged particle identification is based on a likelihood method which assigns a set of probabilities to each

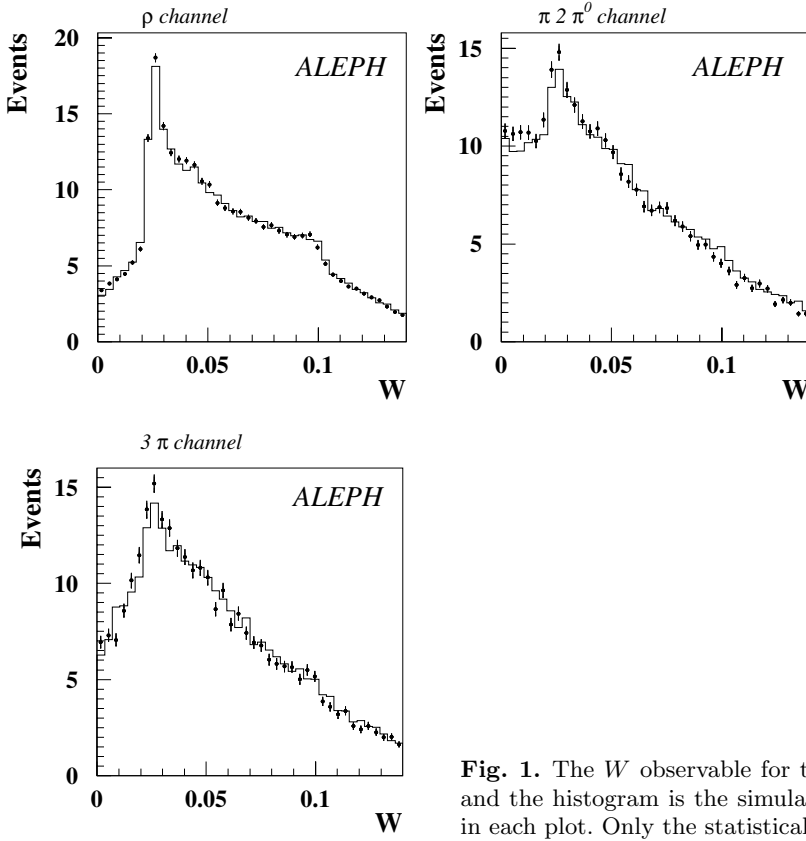


**Fig. 1.** The  $W$  observable for the  $\rho$ ,  $\pi 2 \pi^0$  and  $3 \pi$  decays. The points are the data and the histogram is the simulation. Both distributions are normalised to unit area in each plot. Only the statistical errors are included

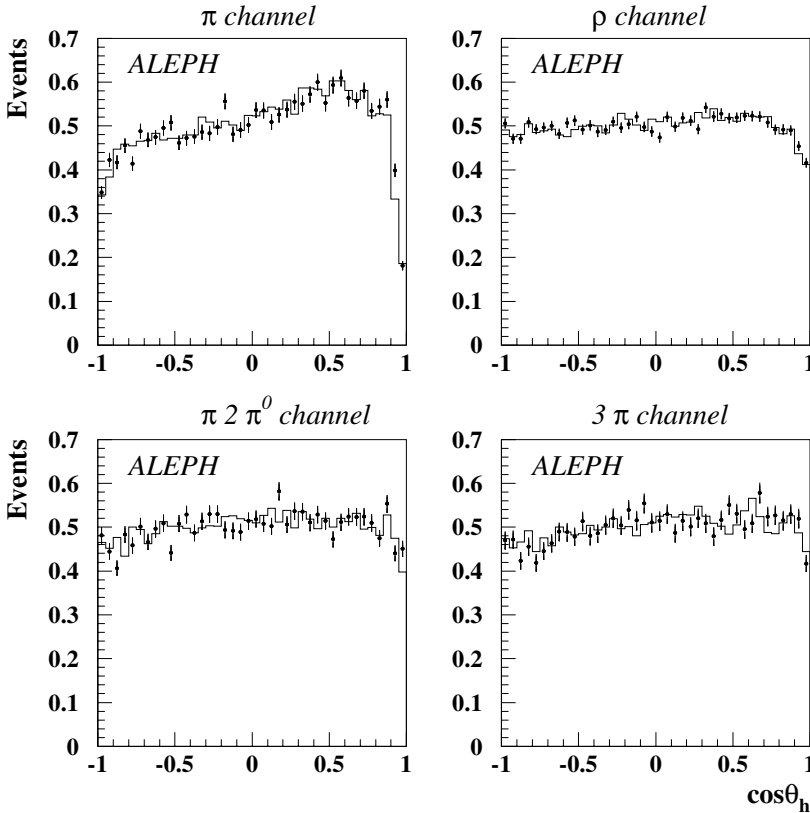


**Fig. 2.** The  $\cos \theta_h$  observable for the four decay topologies. The points are the data and the histogram is the simulation. Both distributions are normalised to unit area in each plot. Only the statistical errors are included

**Table 1.** Selection efficiencies and  $\tau$  background for the different decay channels, obtained from the Monte Carlo simulation and presented with statistical errors only. For this table all identified events are retained

$\tau$ decay	Efficiency (%)	$\tau$ Background (%)
$\pi-\pi$	$57.57 \pm 0.39$	$24.18 \pm 0.39$
$\pi-\pi\pi^0$	$58.39 \pm 0.19$	$21.44 \pm 0.18$
$\pi-\pi 2\pi^0$	$50.36 \pm 0.31$	$34.09 \pm 0.34$
$\pi-3\pi$	$54.29 \pm 0.31$	$16.42 \pm 0.28$
$\pi\pi^0-\pi\pi^0$	$59.76 \pm 0.19$	$19.47 \pm 0.17$
$\pi\pi^0-\pi 2\pi^0$	$52.12 \pm 0.22$	$31.92 \pm 0.23$
$\pi\pi^0-3\pi$	$54.66 \pm 0.21$	$13.96 \pm 0.19$
$\pi 2\pi^0-\pi 2\pi^0$	$45.84 \pm 0.50$	$42.73 \pm 0.56$
$\pi 2\pi^0-3\pi$	$46.98 \pm 0.35$	$27.69 \pm 0.39$
$3\pi-3\pi$	$50.98 \pm 0.48$	$8.57 \pm 0.36$

particle. A detailed description of the method can be found in [6, 7]. The probability set for each particle is obtained from (i) the specific ionisation  $dE/dx$  in the TPC, (ii) the longitudinal and transverse shower profiles in ECAL near the extrapolated track and (iii) the energy and average shower width in HCAL, together with the number of planes fired in the last ten HCAL layers and the number of hits in the muon chambers.

The photon and  $\pi^0$  reconstruction is performed with a likelihood method which first distinguishes between genuine and fake photons produced by hadronic interactions in ECAL or by electromagnetic shower fluctuations [8]. All photon pairs in each hemisphere are then assigned a probability of being generated by a  $\pi^0$ . High energy  $\pi^0$  with overlapping showers are reconstructed through an analysis of the spatial energy deposition in the ECAL towers. All the remaining single photons are considered and those with a high probability of being a genuine photon are selected as  $\pi^0$  candidates. Finally, photon conversions are identified following the procedure described in [8]. They are added to the list of good photons and are included in the  $\pi^0$  reconstruction.

The  $\tau$  decay classification depends on the number of charged tracks and their identification, and on the number of reconstructed  $\pi^0$ . It follows the classification for the measurement of  $P_\tau(\cos\theta_\tau)$  with the  $\tau$  direction method, described in [9] and the references therein.

The  $\tau$  selection efficiencies and the background fractions for the data, presented in Table 1, are estimated from the Monte Carlo simulation. Only statistical errors are quoted. In this data sample the only relevant contamination arises from  $\tau^+\tau^-$  events with misidentified decay modes, referred to as  $\tau$  background.

## 4.2 Tau direction of flight

The reconstruction of the  $\tau$  flight direction is mandatory in this analysis to access the event observables, which are functions of the four-momenta of the final state particles in the  $\tau$  rest frame. This can be achieved in the semileptonic decays, for which the  $\tau$  direction lies on a cone around

**Table 2.** Statistical errors obtained from a Monte Carlo sample approximately equal in size to the data sample, using this analysis and selecting the correct  $\tau$  direction from the information at the generator level

	This analysis	Correct $\tau$ dir.
$\sigma_{\text{Re } \mu_\tau} [10^{-3}]$	0.43	0.34
$\sigma_{\text{Im } \mu_\tau} [10^{-3}]$	0.76	0.58
$\sigma_{\text{Re } d_\tau} [10^{-3}]$	0.39	0.36
$\sigma_{\text{Im } d_\tau} [10^{-3}]$	0.65	0.55

the total hadron momentum. For events with both taus decaying semileptonically the  $\tau$  direction lies along one of the intersection lines of the two reconstructed cones in the case that the taus are produced back-to-back, with equal energies given by  $\sqrt{s}/2$ , and  $m_{\nu_\tau} = m_{\bar{\nu}_\tau} = 0$ . However, the two cones may not intersect due to detector effects or radiation. If the cones intersect, the event is considered twice using either solution. If the cones do not intersect, the particle momenta are fluctuated within their measurement errors and the event is accepted if the cones intersect in a minimum number of trials; the average direction is then used [9].

The effect of using both  $\tau$  directions has been studied with a Monte Carlo sample having approximately the same size as the data. Table 2 presents the statistical errors obtained in this analysis and using the correct  $\tau$  direction from the information at the generator level. Not distinguishing between the two  $\tau$  directions induces some degradation in the overall sensitivity for the four anomalous weak dipole moments.

## 4.3 Candidates and efficiency matrix

The final selection for this analysis requires the  $\tau$  direction to be successfully reconstructed, as described in Sect. 4.2, and the event observables ( $W_1, \cos\theta_{h_1}, \phi_{h_1}, W_2, \cos\theta_{h_2}, \phi_{h_2}$ ) to lie in their domains of validity. These requirements decrease the number of candidates by 21%, the main reason being the inability to reconstruct the  $\tau$  direction for some events.

The final number of candidates in each decay topology is given in Table 3. The efficiency matrix  $\epsilon_{ij}$  for  $i, j = \pi, \rho, \pi 2\pi^0, 3\pi$  is calculated as a function of the generated polar angle  $\cos\theta_h^{(0)}$  separately in the barrel and endcaps; the dependence of  $\epsilon_{ij}$  on  $\phi_h^{(0)}$  and  $W^{(0)}$  is quite uniform and has been integrated out. Figure 3 shows the efficiencies for the barrel. The diagonal elements of this figure represent the identification of each decay mode, while the off-diagonal elements represent its misidentification.

## 4.4 Detector effects

The correct approach to introduce the detector effects in the likelihood formula would be via a smearing function

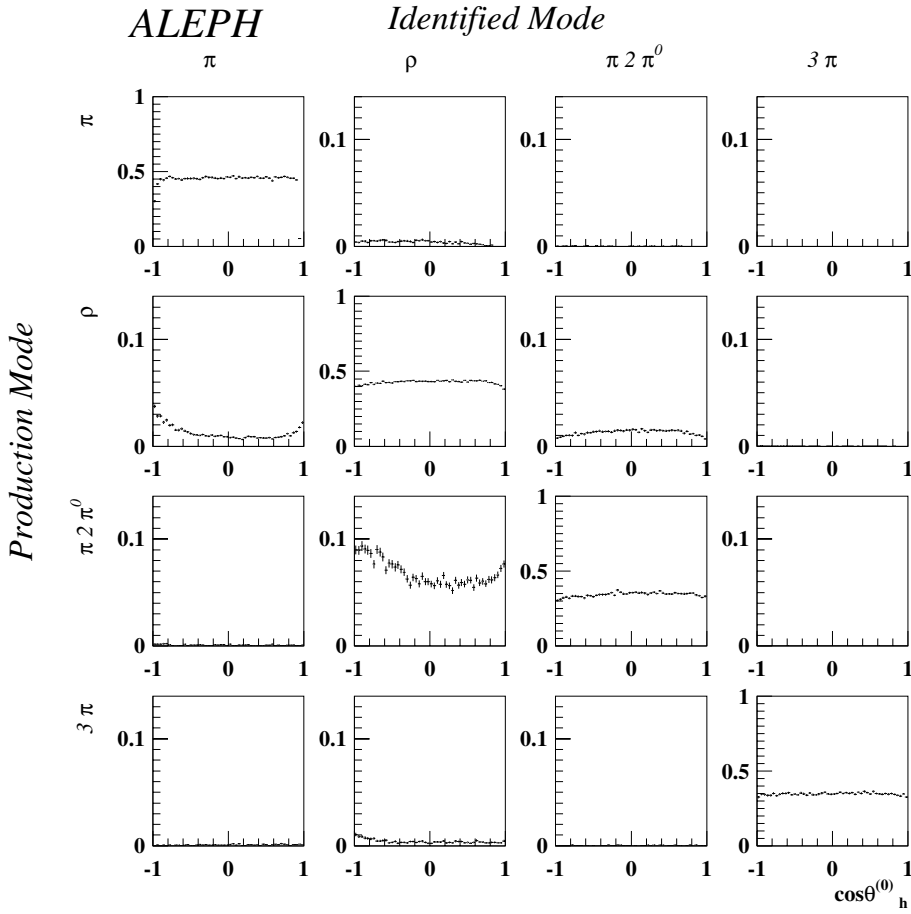


**Fig. 3.** Efficiency function  $\epsilon_{ij}(\cos \theta_h^{(0)})$  in the barrel region

**Table 3.** Number of final candidates in each decay topology and total number of events used in the analysis

Class	Events	Class	Events
$\pi\text{-}\pi$	1901	$\pi\pi^0\text{-}\pi 2\pi^0$	6395
$\pi\text{-}\pi\pi^0$	7844	$\pi\pi^0\text{-}\pi 3\pi$	5242
$\pi\text{-}\pi 2\pi^0$	2673	$\pi 2\pi^0\text{-}\pi 2\pi^0$	1125
$\pi\text{-}3\pi$	2040	$\pi 2\pi^0\text{-}3\pi$	1950
$\pi\pi^0\text{-}\pi\pi^0$	8624	$3\pi\text{-}3\pi$	712
Total number of events: 38506			

$T_{ij}$  depending on 12 variables: the set of event observables and the corresponding generated values. The indices  $i$  and  $j$  indicate the generated and the reconstructed channel, respectively. With the notation used here,

$$T_{ij} = T_{ij} \left( W_1, \cos \theta_{h_1}, \phi_{h_1}, W_2, \cos \theta_{h_2}, \phi_{h_2}, W_1^{(0)}, \cos \theta_{h_1}^{(0)}, \phi_{h_1}^{(0)}, W_2^{(0)}, \cos \theta_{h_2}^{(0)}, \phi_{h_2}^{(0)} \right).$$

Because this function cannot be easily calculated, the detector effects are parametrised by the factorised smearing functions  $D_{ij}(x, x^{(0)})$  for  $x = W, \cos \theta_h$  and by  $D_{ij}^{\cos \theta_h}(x, x^{(0)})$  for  $x = \phi_h$  ( $i, j = \pi, \rho, \pi 2\pi^0, 3\pi$ ). The smearing

function for  $\phi_h$  is calculated in various bins of  $\cos \theta_h$  to take into account correlations between  $\cos \theta_h$  and  $\phi_h$ .

The functions  $D_{ij}(x, x^{(0)})$  give the probability that for generated  $i$  and reconstructed  $j$  the smearing introduced by the detector is  $(x - x^{(0)})$  for a certain generated  $x^{(0)}$  with reconstructed  $x$ . From the definition it follows that

$$\int D_{ij}(x, x^{(0)}) dx = 1. \quad (15)$$

For  $x = \phi_h$  the normalisation is verified in each bin of  $\cos \theta_h$ . These functions are obtained with the SM Monte Carlo simulation by binning the  $(x, x^{(0)})$  plane. The binning has been chosen small enough to correctly convolve detector effects with the generated distribution.

In the likelihood expression, (13), the detector effects are included by replacing the functions  $H_i^\mu$  by

$$\begin{aligned} \tilde{H}_j^\mu(W, \cos \theta_h, \phi_h) &= \sum_i \int H_i^\mu(W^{(0)}, \cos \theta_h^{(0)}, \phi_h^{(0)}) D_{ij}(W, W^{(0)}) \\ &\times D_{ij}(\cos \theta_h, \cos \theta_h^{(0)}) D_{ij}^{\cos \theta_h}(\phi_h, \phi_h^{(0)}) \epsilon_{ij}(\cos \theta_h^{(0)}) \\ &\times dW^{(0)} d\cos \theta_h^{(0)} d\phi_h^{(0)}. \end{aligned} \quad (16)$$

The sum runs over all modes  $i$  which have been reconstructed as one of the modes  $j$  used in the analysis,



**Table 4.** Results of the fit of the calibration curves for each of the decay topologies obtained with the SCOT program and a first order radiator, for  $\mu_\tau$  (top) and for  $d_\tau$  (bottom). The slope  $a$ , the offset  $b$  and the  $\chi^2$  of the linear fit are given for every case. The number of degrees of freedom is three for these linear fits

Channel	Re $\mu_\tau$			Im $\mu_\tau$		
	$a [10^{-2}]$	$b [10^{-4}]$	$\chi^2$	$a [10^{-2}]$	$b [10^{-4}]$	$\chi^2$
$\pi\text{-}\pi$	$76.2 \pm 5.9$	$14.1 \pm 3.8$	3.35	$92.0 \pm 6.3$	$-1.7 \pm 4.3$	0.39
$\pi\text{-}\rho$	$93.3 \pm 2.9$	$12.3 \pm 1.7$	2.28	$68.2 \pm 3.6$	$0.1 \pm 2.2$	5.92
$\pi\text{-}\pi 2\pi^0$	$104.7 \pm 5.3$	$10.2 \pm 3.2$	0.09	$82.8 \pm 6.7$	$0.5 \pm 4.1$	1.63
$\pi\text{-}3\pi$	$108.9 \pm 5.4$	$5.4 \pm 3.2$	0.26	$77.3 \pm 6.8$	$-0.4 \pm 4.2$	2.28
$\rho\text{-}\rho$	$99.1 \pm 3.1$	$9.3 \pm 1.8$	3.64	$60.4 \pm 3.9$	$-1.1 \pm 2.3$	0.84
$\rho\text{-}\pi 2\pi^0$	$99.0 \pm 3.9$	$0.1 \pm 2.3$	0.44	$69.8 \pm 5.0$	$0.8 \pm 3.0$	4.45
$\rho\text{-}3\pi$	$89.7 \pm 3.8$	$0.3 \pm 2.2$	3.55	$60.0 \pm 4.9$	$0.9 \pm 2.8$	4.14
$\pi 2\pi^0\text{-}\pi 2\pi^0$	$96.9 \pm 9.9$	$-3.1 \pm 5.7$	1.72	$60 \pm 14$	$-6.1 \pm 7.9$	0.28
$\pi 2\pi^0\text{-}3\pi$	$89.5 \pm 6.6$	$-0.3 \pm 3.9$	1.75	$73.4 \pm 8.9$	$-1.3 \pm 5.3$	1.10
$3\pi\text{-}3\pi$	$102.0 \pm 9.6$	$-9.6 \pm 5.7$	2.00	$55.0 \pm 12.0$	$-4.0 \pm 7.3$	1.10

Channel	Re $d_\tau$			Im $d_\tau$		
	$a [10^{-2}]$	$b [10^{-4}]$	$\chi^2$	$a [10^{-2}]$	$b [10^{-4}]$	$\chi^2$
$\pi\text{-}\pi$	$76.2 \pm 4.1$	$-1.6 \pm 2.6$	0.25	$51.3 \pm 5.1$	$5.7 \pm 3.1$	0.26
$\pi\text{-}\rho$	$109.4 \pm 2.9$	$1.2 \pm 1.8$	5.82	$90.5 \pm 3.6$	$4.1 \pm 2.3$	4.31
$\pi\text{-}\pi 2\pi^0$	$106.9 \pm 5.4$	$1.3 \pm 3.3$	5.33	$91.4 \pm 7.0$	$4.3 \pm 4.4$	1.17
$\pi\text{-}3\pi$	$113.5 \pm 5.3$	$6.9 \pm 3.3$	1.27	$101.9 \pm 7.0$	$2.2 \pm 4.2$	4.20
$\rho\text{-}\rho$	$109.1 \pm 3.2$	$-3.3 \pm 1.9$	1.83	$80.6 \pm 4.1$	$0.6 \pm 2.4$	2.14
$\rho\text{-}\pi 2\pi^0$	$102.7 \pm 4.0$	$-1.1 \pm 2.3$	1.46	$70.4 \pm 5.2$	$3.0 \pm 3.1$	3.08
$\rho\text{-}3\pi$	$96.4 \pm 3.9$	$1.3 \pm 2.3$	3.76	$60.5 \pm 5.0$	$3.3 \pm 2.9$	1.63
$\pi 2\pi^0\text{-}\pi 2\pi^0$	$96.1 \pm 9.9$	$0.5 \pm 5.8$	0.44	$75 \pm 13$	$2.9 \pm 7.8$	1.08
$\pi 2\pi^0\text{-}3\pi$	$85.2 \pm 6.8$	$4.3 \pm 4.0$	1.59	$66.4 \pm 9.2$	$-1.1 \pm 5.3$	0.16
$3\pi\text{-}3\pi$	$97.0 \pm 10.0$	$2.0 \pm 5.8$	2.48	$60.0 \pm 12.0$	$-2.1 \pm 7.3$	1.73

whereby all possible  $\tau$  decay modes are included in  $i$ . The  $\tau$  branching fractions are taken into account implicitly in (16) because the full differential cross section (13) contains the probability of generating a  $\tau^+\tau^-$  pair decaying into specific decay modes with certain final state topologies.

In terms of the effective functions  $\tilde{H}_i^\mu$  the likelihood for each event reads

$$L_{ij} = \sum_{\mu,\nu=0,\dots,3} \bar{R}_{\mu\nu}(\mu_\tau, d_\tau | \theta_\tau) \tilde{H}_i^\mu(W_1, \cos \theta_{h_1}, \phi_{h_1}) \times \tilde{H}_j^\nu(W_2, \cos \theta_{h_2}, \phi_{h_2}) . \quad (17)$$

#### 4.5 Calibration curves

There are two sources for possible bias in the fitting procedure: (i) the detector effects are handled by the factorised smearing functions  $D_{ij}$  above which take correlations into account only partially, and (ii) radiative corrections are not included in the likelihood. It is thus necessary to evaluate the adequacy of the fitting process. This is done with the SCOT Monte Carlo program [19], interfaced with TAUOLA for the  $\tau$  decays and with the full detector

simulation. The program SCOT describes  $e^+e^- \rightarrow \tau^+\tau^-$  production at an energy around the  $Z$  peak at tree level. It includes the anomalous weak dipole moments and all  $\tau$  spin effects. The initial state radiation is included by adding a simple radiator function [20].

The checks are performed by generating various Monte Carlo samples with different values of the anomalous weak dipole moments. The couplings  $a_e$ ,  $v_e$ ,  $a_\tau$ ,  $v_\tau$  are set to their SM values. The anomalous weak dipole moments Re  $\mu_\tau$ , Im  $\mu_\tau$ , Re  $d_\tau$ , Im  $d_\tau$  are varied one by one in an adequate region around zero. The dependence of the reconstructed values on the generated parameters is taken as linear. Significant deviations of the slopes from unity are found for certain decay topologies, and the offset for Re  $\mu_\tau$  is not consistent with zero for certain channels. These effects have been studied and are mostly related to not using the correct  $\tau$  direction and to background effects. In this analysis, this calibration for each anomalous weak dipole moment and decay topology is taken into account to obtain the corresponding individual measurements. The slopes, offsets and  $\chi^2$  of the linear fits are presented in Table 4.

The offsets and slopes were derived with a Monte Carlo program which includes only a first order radiator for the

**Table 5.** Global differences in the central values of the four anomalous weak dipole moments when using offsets from the KORALZ or SCOT programs

Parameter	Shift
$\text{Re } \mu_\tau [10^{-3}]$	$-0.45 \pm 0.21$
$\text{Im } \mu_\tau [10^{-3}]$	$-0.43 \pm 0.42$
$\text{Re } d_\tau [10^{-3}]$	$0.05 \pm 0.19$
$\text{Im } d_\tau [10^{-3}]$	$0.81 \pm 0.38$

initial state bremsstrahlung. The offsets have then been verified with the KORALZ Monte Carlo program [21] interfaced with the full detector simulation. KORALZ describes  $e^+e^- \rightarrow \tau^+\tau^-$  production at an energy around the  $Z$  peak and with initial state bremsstrahlung corrections up to  $O(\alpha^2)$ , final state  $O(\alpha)$  bremsstrahlung and  $O(\alpha)$  electroweak corrections. However, this program contains only longitudinal spin effects (i.e., the production terms used are  $R_{00}$ ,  $R_{03}$  and  $R_{33}$ ) and the anomalous weak dipole moments are set to zero. To check the effect of this approximation, a maximum likelihood fit was built to include the complete  $R_{00}$ ,  $R_{03}$  and  $R_{33}$  terms and the anomalous parts of the other  $R_{\mu\nu}$  terms. The values obtained for the four anomalous weak dipole moments for each decay topology are consistent with the corresponding offsets computed with SCOT and the first order radiator. Table 5 shows the global differences between the offsets of the central values of the four anomalous weak dipole moments when using either KORALZ or SCOT. The final results of this analysis are obtained by correcting the individual measurements according to the KORALZ offsets and the SCOT slopes and by including the statistical error of the correction in the systematic uncertainty. The statistical error of the SCOT offsets is also included in the systematic uncertainty as these offsets have contributions from all  $R_{\mu\nu}$  terms.

## 5 Systematic uncertainties

The systematic uncertainty is calculated for each anomalous weak dipole moment and final state decay topology. The estimates are shown in Tables 6 to 9. The last row of these tables shows the combined systematic uncertainty from each source taking into account the correlations between channels.

The ECAL effects are related to the uncertainty in the global energy scale and the nonlinearity of the response. The global scale is known at the level of 0.25%, through the calibration with Bhabha events. Global variations have been applied to each ECAL module and the effect is propagated to the fitted parameters. The nonlinearity of the response is related to the wire saturation constants of ECAL, which are different in the barrel and endcaps. These saturation constants have been fluctuated within their nominal errors while keeping the measured energy fixed at  $M_Z/2$ .

The TPC systematic errors are related to the momentum measurement: (i) an effect due to the magnetic field acting similarly on positive and negative charged tracks, and (ii) a sagitta effect affecting oppositely positive and negative tracks. These two effects are calibrated with dimuon events and the corresponding corrections are applied to the  $\tau$  data. The systematic errors are then estimated by varying the corrections within their errors for each year.

The systematic errors in the column labeled “Align.” are due to a possible azimuthal tilt between the different parts of the detector.

Variations in the  $\tau$  branching fractions are considered in the  $\tau$ BF column. This systematic uncertainty was determined from its effect on the calibration curves (Sect. 4.5).

The experimental errors on the weak parameters  $\sin^2 \theta_W$  and  $M_Z$  are propagated to the fitted values. Other weak parameters have negligible effect on the measurements. These effects are summarised in the column labeled “Wpar”.

The finite Monte Carlo statistics also causes systematic uncertainties. The most relevant statistical uncertainty is for the KORALZ offsets. The statistical error of the offsets and slopes obtained with SCOT and the first order radiator (Table 4) are also taken into account. Finally, the statistical error in the calculation of the efficiency matrix is also considered. These effects are shown under the column “MC st.”.

The  $a_1$  decay dynamics are not well described theoretically. The impact of this was evaluated in the past [22] by implementing several models in the analysis [23]. The implementation of those models is much more difficult in the present analysis. The uncertainty is estimated by means of three models: the Kühn & Santamaria (KS) model [24] (used in the fitting formula), the Feindt model [25] and the Isgur, Morningstar and Reader (simplified) model [26]. The effects of the Feindt and IMR models on  $W$  and  $h^3$  are calculated. The corresponding ratios with the  $W$  and the  $h^3$  of the KS model are then used to scale the error.

Another source of systematic error is due to fake photons generated by hadron interactions in the ECAL or by electromagnetic fluctuations. This quantity of photon candidates is underestimated in the Monte Carlo simulation compared to the data. This deficit was originally observed in a substantial disagreement between the data and the Monte Carlo simulation for the  $W$  distribution in the  $\pi 2\pi^0$  channel. This discrepancy has notably decreased after weighting the events of the Monte Carlo simulation according to the number of fake photons. This weighting was optimised for other  $\tau$  analyses [9]. Figure 1 compares the  $W$  distributions for the data and the Monte Carlo after the approximate weighting. In the end, the effect of fake photons is taken into account by removing fake photons in the simulation and using the difference in the fitted parameters as systematic uncertainty.

The total systematic error and the statistical error for each channel and parameter are shown in the last two columns of the tables.

**Table 6.** Systematic uncertainties on  $\text{Re } \mu_\tau$  for the different channels. The last row gives the combined systematic uncertainty from each source taking into account the correlations between channels. The total systematic and statistical errors are shown in the last two columns. The values are expressed in units of  $[10^{-4}]$ . The sources of uncertainty are explained in the text

	ECAL	TPC	Align.	$\tau$ BF	Wpar	MC st.	$a_1$ dyn.	Fake $\gamma$	$\sigma_{\text{sys}}$	$\sigma_{\text{stat}}$
$\pi$ - $\pi$	4.53	0.84	0.58	1.55	0.11	14.30	0.	2.88	15.39	24.70
$\pi$ - $\rho$	2.90	0.48	0.04	0.25	0.12	4.64	0.	0.23	5.51	9.35
$\pi$ - $\pi 2\pi^0$	2.77	2.98	0.12	1.12	0.06	7.52	0.45	0.54	8.65	14.81
$\pi$ - $3\pi$	0.63	12.23	6.95	0.43	0.14	7.39	1.23	0.85	15.98	16.58
$\rho$ - $\rho$	2.63	1.23	0.28	0.37	0.11	4.43	0.	0.64	5.36	8.45
$\rho$ - $\pi 2\pi^0$	3.20	0.53	0.42	0.61	0.06	5.53	1.88	1.54	6.90	11.67
$\rho$ - $3\pi$	1.55	1.38	1.94	0.60	0.08	5.87	0.61	1.60	6.77	11.37
$\pi 2\pi^0$ - $\pi 2\pi^0$	10.24	1.72	0.86	1.49	0.14	13.56	11.37	2.03	20.69	22.75
$\pi 2\pi^0$ - $3\pi$	4.50	3.04	2.38	1.62	0.03	10.07	2.91	1.31	12.22	20.31
$3\pi$ - $3\pi$	1.65	7.82	7.62	0.89	0.24	13.17	4.69	4.61	18.43	25.55
Combined	0.72	0.92	0.43	0.17	0.08	2.19	0.43	0.18	2.60	4.20

**Table 7.** Systematic uncertainties on  $\text{Im } \mu_\tau$  for the different channels. The last row gives the combined systematic uncertainty from each source taking into account the correlations between channels. The total systematic and statistical errors are shown in the last two columns. The values are expressed in units of  $[10^{-4}]$ . The sources of uncertainty are explained in the text

	ECAL	TPC	Align.	$\tau$ BF	Wpar	MC st.	$a_1$ dyn.	Fake $\gamma$	$\sigma_{\text{sys}}$	$\sigma_{\text{stat}}$
$\pi$ - $\pi$	1.60	0.86	0.42	0.43	0.09	13.29	0.	0.97	13.46	25.06
$\pi$ - $\rho$	0.86	0.38	1.52	0.39	0.05	8.11	0.	2.44	8.66	16.60
$\pi$ - $\pi 2\pi^0$	27.55	3.40	3.03	1.58	0.39	14.92	8.75	3.24	33.05	29.65
$\pi$ - $3\pi$	11.23	9.64	9.98	0.61	0.27	15.72	8.94	0.	25.42	32.96
$\rho$ - $\rho$	3.29	0.13	0.85	0.64	0.09	10.21	0.	1.09	10.84	18.09
$\rho$ - $\pi 2\pi^0$	32.05	2.98	1.13	0.56	0.06	12.51	2.01	8.19	35.57	25.10
$\rho$ - $3\pi$	9.60	1.51	0.57	1.43	0.08	12.70	2.04	10.85	19.40	21.85
$\pi 2\pi^0$ - $\pi 2\pi^0$	100.21	2.20	6.70	5.49	0.57	35.31	7.17	10.17	107.35	62.38
$\pi 2\pi^0$ - $3\pi$	17.50	11.90	5.75	1.14	0.22	17.61	12.21	15.62	34.43	37.88
$3\pi$ - $3\pi$	5.38	5.70	1.66	0.99	0.31	34.50	10.76	17.05	40.77	64.46
Combined	4.27	0.17	0.30	0.23	0.05	4.18	1.12	0.76	6.10	8.00

**Table 8.** Systematic uncertainties on  $\text{Re } d_\tau$  for the different channels. The last row gives the combined systematic uncertainty from each source taking into account the correlations between channels. The total systematic and statistical errors are shown in the last two columns. The values are expressed in units of  $[10^{-4}]$ . The sources of uncertainty are explained in the text

	ECAL	TPC	Align.	$\tau$ BF	Wpar	MC st.	$a_1$ dyn.	Fake $\gamma$	$\sigma_{\text{sys}}$	$\sigma_{\text{stat}}$
$\pi$ - $\pi$	1.27	0.58	0.09	0.77	0.12	8.33	0.	0.16	8.48	15.61
$\pi$ - $\rho$	0.18	0.40	0.61	0.35	0.04	3.91	0.	4.51	6.03	7.94
$\pi$ - $\pi 2\pi^0$	8.38	1.73	1.58	1.78	0.09	7.68	3.36	3.21	12.63	15.34
$\pi$ - $3\pi$	1.36	0.57	0.02	0.27	0.02	7.22	2.71	1.00	7.92	15.05
$\rho$ - $\rho$	0.53	0.35	0.49	0.38	0.04	4.18	0.	0.17	4.28	8.04
$\rho$ - $\pi 2\pi^0$	1.45	1.68	0.63	0.79	0.08	5.39	0.79	2.63	6.52	10.89
$\rho$ - $3\pi$	5.37	1.68	0.79	0.45	0.	5.56	3.00	2.26	8.80	10.89
$\pi 2\pi^0$ - $\pi 2\pi^0$	8.75	2.00	1.10	1.71	0.07	13.35	8.18	9.44	20.47	29.74
$\pi 2\pi^0$ - $3\pi$	5.26	12.07	10.96	2.56	0.05	10.39	4.88	3.75	21.11	21.65
$3\pi$ - $3\pi$	1.91	4.75	4.70	1.64	0.12	14.06	5.34	2.25	16.80	29.39
Combined	0.41	0.29	0.26	0.17	0.02	1.94	0.90	0.50	2.30	3.90

**Table 9.** Systematic uncertainties on  $\text{Im } d_\tau$  for the different channels. The last row gives the combined systematic uncertainty from each source taking into account the correlations between channels. The total systematic and statistical errors are shown in the last two columns. The values are expressed in units of  $[10^{-4}]$ . The sources of uncertainty are explained in the text

	ECAL	TPC	Align.	$\tau$ BF	Wpar	MC st.	$a_1$ dyn.	Fake $\gamma$	$\sigma_{\text{sys}}$	$\sigma_{\text{stat}}$
$\pi$ - $\pi$	1.02	0.59	0.65	1.25	0.06	14.95	0.	5.01	15.87	26.10
$\pi$ - $\rho$	2.48	0.74	0.41	0.16	0.08	6.90	0.	0.94	7.44	13.63
$\pi$ - $\pi 2\pi^0$	51.04	6.50	2.73	1.14	0.81	15.60	8.59	5.29	54.79	29.55
$\pi$ - $3\pi$	3.47	3.38	5.14	0.79	0.14	11.90	4.30	8.03	16.59	23.50
$\rho$ - $\rho$	2.91	0.60	0.55	0.63	0.04	8.54	0.	0.26	9.09	15.07
$\rho$ - $\pi 2\pi^0$	17.69	0.44	0.29	1.20	0.08	12.46	6.52	2.54	22.78	24.64
$\rho$ - $3\pi$	6.09	9.99	5.87	0.36	0.07	12.40	1.04	5.91	19.01	23.31
$\pi 2\pi^0$ - $\pi 2\pi^0$	9.86	10.57	17.41	3.38	1.15	28.17	40.10	14.34	55.96	72.95
$\pi 2\pi^0$ - $3\pi$	8.12	7.21	3.72	4.21	0.11	19.32	1.73	6.86	23.93	41.51
$3\pi$ - $3\pi$	4.46	12.78	8.80	0.67	0.29	30.10	7.80	4.19	35.30	59.22
Combined	5.74	1.80	0.70	0.32	0.04	3.80	0.79	0.43	7.20	7.20

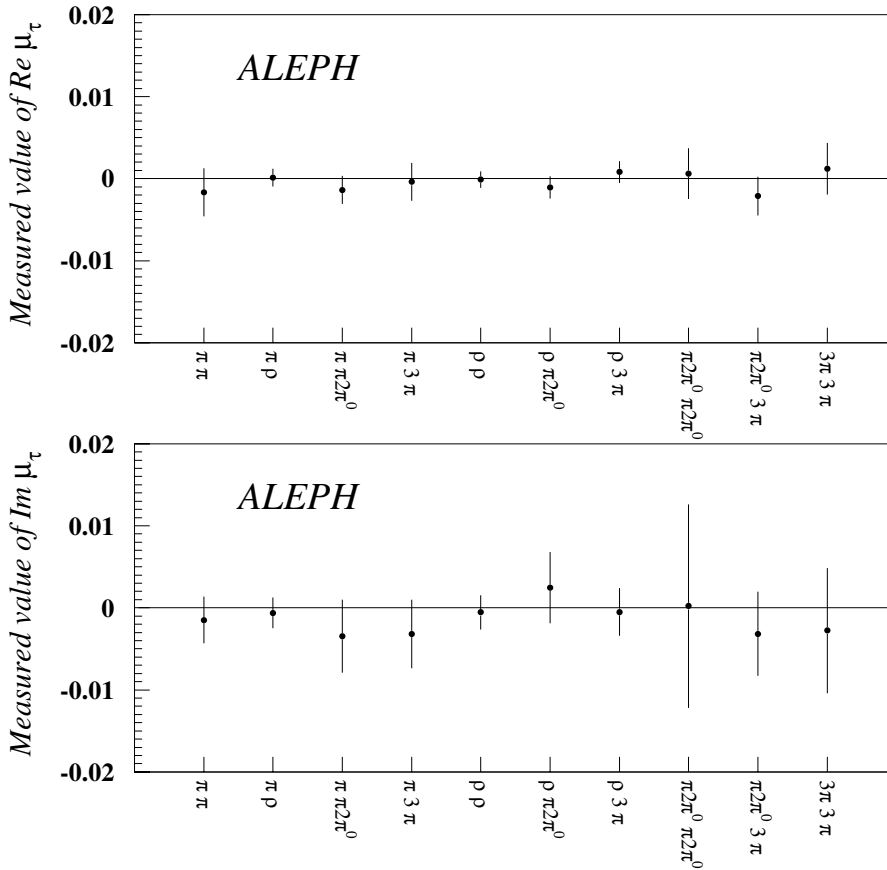


**Fig. 4.** Results on  $\mu_\tau$  for the various decay modes, including both the statistical and the systematic uncertainties. The results on  $\text{Re } \mu_\tau$  are shown at the top, and on  $\text{Im } \mu_\tau$  at the bottom

## 6 Results and conclusions

The final individual measurements of the four anomalous weak dipole moments are obtained applying the offsets and slopes described in Sect. 4.5. The results for the different decay topologies are presented in Figs. 4 and 5, including both the systematic and the statistical errors. All these measurements are consistent with the SM prediction. Figure 6 shows the relative weights of the differ-

ent decay channels for the four measured anomalous weak dipole moments.

The final combined results on the four anomalous weak dipole moments are listed in Table 10, showing the statistical, systematic and total errors. The statistical correlations are given in Table 11. The final 95% CL upper limits derived from these measurements are presented in Table 12.

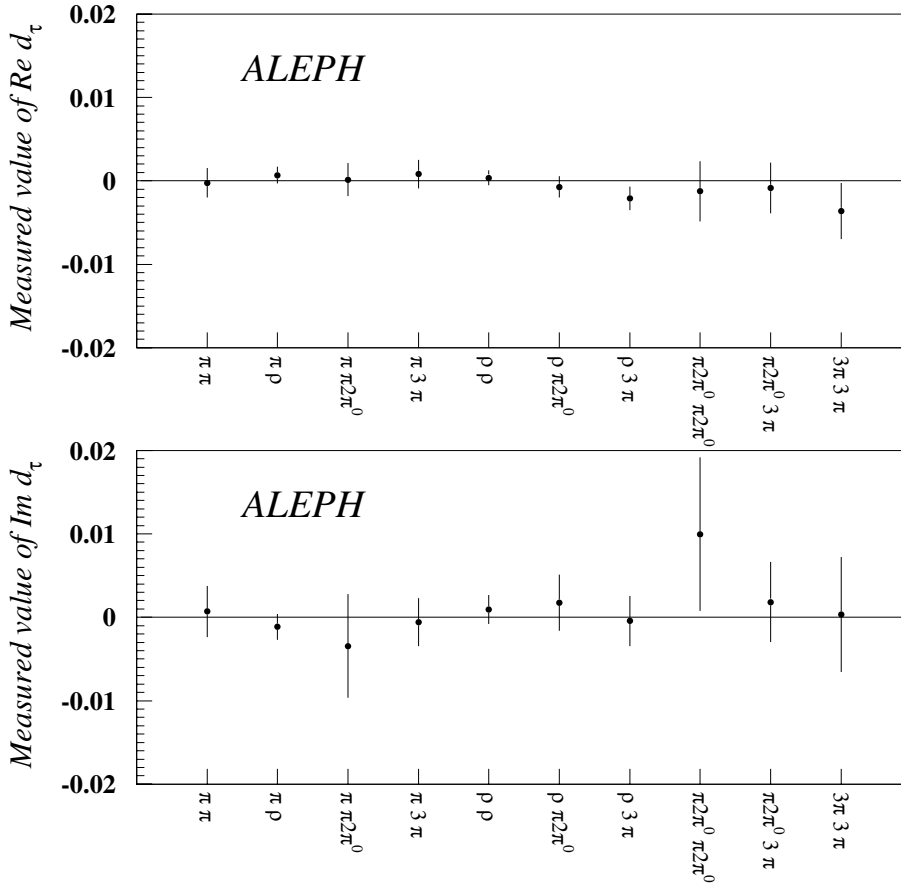


**Fig. 5.** Results on  $d_\tau$  for the various decay modes, including both the statistical and the systematic uncertainties. The results on  $\text{Re } d_\tau$  are shown at the top, and on  $\text{Im } d_\tau$  at the bottom. The anomalous weak electric dipole moment is assumed dimensionless in these figures

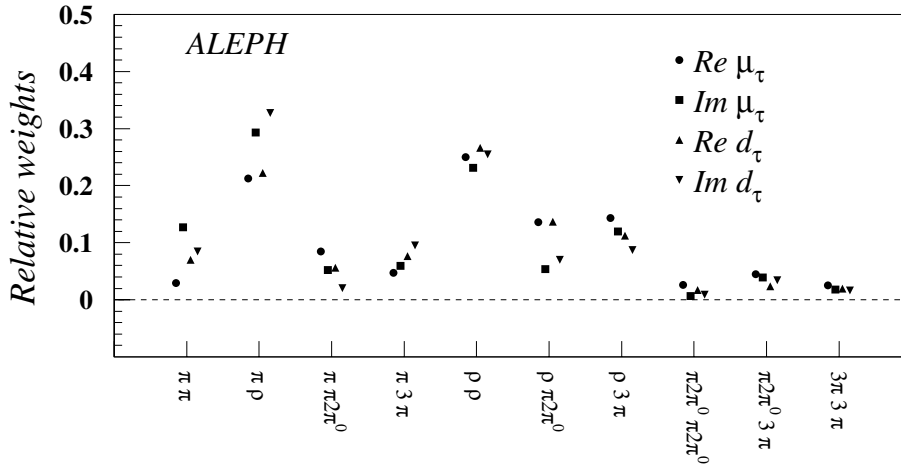


**Fig. 6.** Relative weights of the different decay topologies for the four measured anomalous weak dipole moments, normalised to the total weight

**Table 10.** Final results on the real and imaginary terms of the anomalous weak dipole moments

Parameter	Fitted value	$\sigma_{\text{stat}}$	$\sigma_{\text{sys}}$	$\sigma$
$\text{Re } \mu_\tau [10^{-3}]$	-0.33	0.42	0.26	0.49
$\text{Im } \mu_\tau [10^{-3}]$	-0.99	0.80	0.61	1.01
$\text{Re } d_\tau [10^{-3}] ([10^{-18} \text{e cm}])$	-0.11 (-0.59)	0.39 (2.14)	0.23 (1.26)	0.45 (2.49)
$\text{Im } d_\tau [10^{-3}] ([10^{-18} \text{e cm}])$	-0.08 (-0.45)	0.72 (4.00)	0.72 (4.01)	1.02 (5.67)

**Table 11.** Statistical correlations between the fitted parameters. The individual correlations are presented in the off-diagonal elements

	$\text{Re } \mu_\tau$	$\text{Im } \mu_\tau$	$\text{Re } d_\tau$	$\text{Im } d_\tau$
$\text{Re } \mu_\tau$	1.0	0.006	0.028	0.062
$\text{Im } \mu_\tau$		1.0	-0.055	0.034
$\text{Re } d_\tau$			1.0	-0.003
$\text{Im } d_\tau$				1.0

**Table 12.** Upper limits derived from this measurement of the anomalous weak dipole moments (95% CL)

Parameter	Limit
$ \text{Re } \mu_\tau  [10^{-3}]$	1.14
$ \text{Im } \mu_\tau  [10^{-3}]$	2.65
$ \text{Re } d_\tau  [10^{-3}] ([10^{-18} \text{ e cm}])$	0.91 (5.01)
$ \text{Im } d_\tau  [10^{-3}] ([10^{-18} \text{ e cm}])$	2.01 (11.15)

These results supersede the previous ALEPH measurement of  $\text{Re } d_\tau$  [3]; the measurement of  $\text{Re } \mu_\tau$ ,  $\text{Im } \mu_\tau$  and  $\text{Im } d_\tau$ , presented in this paper gives the most stringent limits on these quantities to date.

*Acknowledgements.* We wish to thank our colleagues from the accelerator divisions for the successful operation of LEP. We are indebted to the engineers and technicians in all our institutions for their contribution to the good performance of ALEPH. Those of us from non-member states thank CERN for its hospitality.

## References

1. J. Bernabéu, G.A. González-Springberg, M. Tung, J. Vidal, Nucl. Phys. B **436**, 474 (1995)
2. W. Bernreuther, U. Löw, J.P. Ma, O. Nachtmann, Z. Phys. C **43**, 117 (1989)
3. ALEPH Collaboration, Search for CP violation in  $Z \rightarrow \tau^+\tau^-$ , Phys. Lett. B **297**, 459 (1992) ; Search for CP violation in the decay  $Z \rightarrow \tau^+\tau^-$ , Phys. Lett. B **346**, 371 (1995)
4. OPAL Collaboration, Test of CP-invariance in  $e^+e^- \rightarrow Z^0 \rightarrow \tau^+\tau^-$  and a limit on the weak dipole moment of the tau lepton, Phys. Lett. B **281**, 405 (1992) ; A test of CP-invariance in  $Z^0 \rightarrow \tau^+\tau^-$  using optimal observables, Z. Phys. C **66**, 31 (1995) ; Search for CP violation in  $Z^0 \rightarrow \tau^+\tau^-$  and an upper limit on the weak dipole moment of the tau lepton, Z. Phys. C **74**, 403 (1997)
5. L3 Collaboration, Measurement of the weak dipole moments of the  $\tau$  lepton, Phys. Lett. B **426**, 207 (1998)
6. ALEPH Collaboration, Measurement of  $\tau$  branching ratios, Z.Phys. C **54**, 211 (1992)
7. ALEPH Collaboration, Tau leptonic branching ratios, Z.Phys. C **70**, 561 (1996)
8. ALEPH Collaboration, Tau hadronic branching ratios, Z.Phys. C **70**, 579 (1996)
9. ALEPH Collaboration, Measurement of the tau polarisation at LEP I, Eur. Phys. J. C **20**, 401 (2001)
10. U. Stiegler, Z.Phys. C **58**, 601 (1993)
11. The ALEPH Collaboration, Measurement of the Z resonance parameters at LEP, Eur. Phys. J. C **14**, 1 (2000)
12. ALEPH Collaboration, Measurement of the transverse spin correlations in the decay  $Z \rightarrow \tau^+\tau^-$ , Phys. Lett. B **405**, 191 (1997)
13. F. Sánchez, Phys. Lett. B **412**, 137 (1997)
14. S. Jadach, J.H. Kühn, Z. Wąs, Comput. Phys. Commun. **64**, 275 (1991) ; S. Jadach, J.H. Kühn, Z. Wąs, R. Decker, Comput. Phys. Commun. **76**, 361 (1993)
15. J. Bernabéu, A. Pich, N. Rius, Phys. Lett. B **257**, 219 (1991) ; R. Alemany et al., Nucl. Phys. B **379**, 3 (1992)
16. S. Jadach, Z. Wąs, Acta Physica Polonica B **15**, 1151 (1984)
17. ALEPH Collaboration, ALEPH: A Detector for Electron-Positron Annihilations at LEP, Nucl. Inst. and Meth. A **294**, 121 (1990)
18. ALEPH Collaboration, Performance of the ALEPH detector at LEP, Nucl. Inst. and Meth. A **360**, 481 (1995)
19. U. Stiegler, Comput. Phys. Commun. **81**, 221 (1994)
20. G. Bonneau, F. Martin, Nucl. Phys. B **27**, 381 (1971) ; R. Miquel, Radiative corrections to the process  $e^+e^- \rightarrow \nu\nu\gamma$ , Ph.D. thesis, Universitat Autònoma de Barcelona (1989)
21. S. Jadach, Z. Wąs, B.F.L. Ward, Comput. Phys. Commun. **66**, 276 (1991)
22. ALEPH Collaboration, Improved  $\tau$  polarization measurement, Z.Phys. C **69**, 183 (1996)
23. L. Duflot, Nouvelle méthode de mesure de la polarisation du  $\tau$ . Application au canal  $\tau \rightarrow a_1\nu_\tau$  dans l'expérience ALEPH, Ph.D. thesis, Université de Paris-Sud, Centre d'Orsay (1993)
24. J.H. Kühn, A. Santamaria,  $\tau$  decays to pions, Munich preprint MPIPAE/PTh 17/90
25. M. Feindt, Z. Phys. C **48**, 681 (1990)
26. N. Isgur et al., Phys. Rev. D **39**, 1357 (1989)